Ultrasound in Med. & Biol., Vol. 27, No. 4, pp. 535–550, 2001

0301-5629/01/$–see front matter

PII: S0301-5629(00)00361-6

● *Original Contribution*

PERFORMANCE OF TIME-FREQUENCY REPRESENTATION TECHNIQUES TO MEASURE BLOOD FLOW TURBULENCE WITH PULSED-WAVE DOPPLER ULTRASOUND

GUY CLOUTIER,*†‡ DANMIN CHEN,* LOUIS-GILLES DURAND*

*Laboratory of Biomedical Engineering, Institut de recherches cliniques de Montréal; †Laboratory of Biorheology and Medical Ultrasonics, Centre Hospitalier de l'Université de Montréal; and ‡Department of Radiology, Université de Montréal, Montréal, Québec, Canada

(*Received* 12 *July* 2000; *in final form* 20 *November* 2000)

Abstract—The current processing performed by commercial instruments to obtain the time-frequency representation (TFR) of pulsed-wave Doppler signals may not be adequate to characterize turbulent flow motions. The assessment of the intensity of turbulence is of high clinical importance and measuring high-frequency (small-scale) flow motions, using Doppler ultrasound (US), is a difficult problem that has been studied very little. The objective was to optimize the performance of the spectrogram (SPEC), autoregressive modeling (AR), Choi–Williams distribution (CWD), Choi–Williams reduced interference distribution (CW-RID), Bessel distribution (BD), and matching pursuit method (MP) for mean velocity waveform estimation and turbulence detection. The intensity of turbulence was measured from the fluctuations of the Doppler mean velocity obtained from a simulation model under pulsatile flow. The Kolmogorov spectrum, which is used to determine the frequency of the fluctuations and, thus, the scale of the turbulent motions, was also computed for each method. The best set of parameters for each TFR method was determined by minimizing the error of the absolute frequency fluctuations and Kolmogorov spectral bandwidth measured from the simulated and computed Doppler spectra. The results showed that different parameters must be used for each method to minimize the velocity variance of the estimator, to optimize the detection of the turbulent frequency fluctuations, and to estimate the Kolmogorov spectrum. To minimize the variance and to measure the absolute turbulent frequency fluctuations, four methods provided similar results: SPEC (10-ms sine-cosine windows), AR (10-ms rectangular windows, model order = 8), CWD (w_N and w_M = 10-ms rectangular windows, $\sigma = 0.01$), and BD (w_N = 10-ms rectangular windows, $\alpha = 16$). The velocity variance in the absence of turbulence was on the order of 0.04 m/s (coefficient of variation ranging from 8.0% to 14.5%, depending on the method). With these spectral techniques, the peak of the turbulence intensity was adequately estimated (velocity bias < 0.01 m/s). To track the frequency of turbulence, the best method was BD (w_N = 2-ms rectangular windows, $\alpha = 2$). The bias in the estimate of the −10 dB bandwidth of the Kolmogorov spectrum was 354 ± 51 Hz in the absence of turbulence (the true bandwidth should be 0 Hz), and −193 ± 371 Hz with turbulence (the simulated −10-dB bandwidth was estimated at 1256 Hz instead of 1449 Hz). In conclusion, several TFR methods can be used to measure the magnitude of the turbulent fluctuations. To track eddies ranging from large vortex to small turbulent fluctuations (wide Kolmogorov spectrum), the Bessel distribution with appropriate set of parameters is recommended. (E-mail: cloutig@ircm.qc.ca)

Key Words: **Ultrasonography, Echocardiography, Simulation, Spectral methods, Heart valve disease, Insufficiency, Regurgitation, Stenosis, Turbulence, Reynolds stress.**

INTRODUCTION

Turbulence is an irregular eddying motion in time and space characterized by velocity and pressure fluctuations about their mean values. These turbulent fluctuations are made of eddies of different sizes within larger eddies. Pathophysiologically, at a given flow rate, turbulence increases the flow resistance and the wall shear rate compared to laminar flow (Milnor 1989). In the cardiovascular system, turbulence has been associated with poststenotic dilatation, aneurysms, atherogenesis and thrombosis (Nichols and O'Rourke 1990). A region of the cardiovascular system where turbulence plays a significant role is the ascending thoracic aorta distal to the

Address correspondence to: Dr. Cloutier, Laboratory of Biomedical Engineering, Institut de recherches cliniques de Montréal, 110 avenue des Pins Ouest, Montréal, Québec, Canada, H2W 1R7. E-mail: cloutig@ircm.qc.ca

aortic heart valve. Thrombogenic complications after replacement of diseased heart valves with mechanical prostheses have been shown to be related to the hemodynamics in the vicinity of the valve, namely flow stasis and turbulent high shear stresses (Butchart 1998; Chesebro and Fuster 1998). One mechanism by which turbulence promotes thrombogenic complications in patients with mechanical heart valve substitutes is the effect of turbulent Reynolds stresses on the rupture of erythrocytes (Sallam and Hwang 1984) and platelets (Hung et al. 1976) and, possibly, on the function of endothelial cells (Stein et al. 1977). The release of adenosine diphosphate by ruptured blood cells or simply the shearing effect can promote platelet aggregation, adhesion to the endothelium and thrombosis (Butchart 1998; Kroll et al. 1996).

According to the literature, very few studies have investigated the accuracy of Doppler ultrasound (US) to track turbulent velocity motions. Giddens and Khalifa (1982) proposed a phase-lock loop frequency-tracking method to measure the time fluctuations of the Doppler mean velocity. This approach was applied to study poststenotic flow disturbances in dogs (Talukder et al. 1986). The time resolution of their instrumentation was greater than 5 ms. Zero-crossing detectors, providing a time resolution on the order of 2.5 ms, were proposed to map turbulent velocity fluctuations within the aorta of patients with mechanical heart valves (Nygaard et al. 1994b). The system developed by this group uses a cuff containing five Doppler probes in contact with surgically exposed aortas (Nygaard et al. 1994a). Today, although better time resolutions can be achieved with commercial US instruments, the variance of the time-frequency representation (TFR) method used to compute the real-time Doppler spectrum may not allow turbulent motions to be efficiently detected.

To our knowledge, the detection of random turbulent fluctuations covering a wide range of eddy sizes has not been addressed in the US literature. For the purpose of measuring turbulence produced by prosthetic heart valves *in vivo*, this is an important objective to achieve because blood cell hemolysis and thrombosis may not only be related to the turbulence intensity and duration of exposure, but also to the scale of the turbulent fluctuations. Clinical studies aiming at evaluating the relationship between turbulence stresses and thrombogenic complications in patients after heart valve replacement cannot be performed with the current technologies. Only US can provide such a tool for noninvasive studies in patients. The magnetic resonance imaging (MRI) technology is currently under development and may eventually represent an alternative to US (Fontaine et al. 1996; Walker et al. 1995).

Two basic criteria have to be optimized for obtaining an optimum mean frequency computed from the Doppler spectrum. First, the variance of the TFR method has to be low to avoid an overestimation of the turbulence intensity, and second, it is mandatory to have a technique with a good time-frequency resolution to allow the detection of fast turbulent fluctuations. Of course, a signal $x(n)$ cannot simultaneously be time-limited and bandlimited. The selection of the optimum TFR method should be based on a compromise between time and frequency resolutions. In the current study, the variance and accuracy of six TFR methods to track turbulent random fluctuations were evaluated with a simulation model of the Doppler cardiac signal.

METHODS

Time-frequency representation methods tested

The Spectrogram. The spectrogram is a traditional method of analyzing a signal in the joint time-frequency domain. It provides the TFR of the signal $x(n)$, at the discrete time n, by computing the power spectrum of a small segment of the signal around n. It is computed by using the discrete Fourier transform (DFT) as follow:

$$SPEC_x(n,k) = \left| \sum_{\tau=-\infty}^{+\infty} e^{-j2\pi k\tau/N} x(\tau) w(\tau - n) \right|^2, \quad (1)$$

where n and k correspond to the discrete time and frequency variables, respectively, j is the imaginary number, N is the number of samples of the signal $x(n)$, and $w(\tau)$ is a window function.

Autoregressive modeling. This method is similar to the spectrogram, except that the DFT of each segment of the signal $x(n)$ is replaced by an autoregressive (*AR*) model given by:

$$AR_x(n,k) = \frac{\delta_p^2(n)}{\left| 1 + \sum_{m=1}^{p} a(m,n) \exp\left(-j \frac{2\pi k}{N} m \right) \right|^2}, \quad (2)$$

where $\delta_p^2(n)$ is the variance of the modeling error signal corresponding to the model order p. The complex time-varying coefficients $a(m,n)$ are computed by using the Yule–Walker equations together with the Levinson–Durbin algorithm for an efficient recursive solution. The time window $w(\tau)$ is applied to the signal $x(n)$, at the time n, to extract a small segment before computing the coefficients $a(m)$. More details on this algorithm can be found in Kay and Marple (1981)).

The Choi–Williams distribution. Choi and Williams (1989) introduced a bilinear distribution by using an exponential kernel $\Phi(\xi, \tau) = e^{-(\xi^2\tau^2)/\sigma}$. It is a member of a group of time-frequency distributions (Cohen group) individually characterized by a cross-term suppressing time-frequency smoothing kernel function. The Choi–Williams distribution is given by (Jeong and Williams 1992a):

$$CWD_x(n,k) = 2\sum_{\tau=-\infty}^{+\infty} w_N(\tau)e^{-j2\pi k\tau/N}\left[\sum_{\mu=-\infty}^{+\infty} w_M(\mu)\frac{1}{\sqrt{4\pi\tau^2/\sigma}}\exp\left(-\frac{(2\mu+\tau)^2}{16\tau^2/\sigma}\right)x(n+\mu+\tau)x^*(n+\mu)\right], \quad (3)$$

where $w_N(\tau)$ is a symmetric window having nonzero values within the range of $-N/2 \le \tau \le N/2$, $w_M(\mu)$ is a rectangular window that has a value of 1 between $-M/2 \le \mu \le M/2$, the parameter σ is used to trade-off auto-term resolution for cross-term suppression, and * indicates the complex conjugate.

The Choi–Williams reduced interference distribution. Jeong and Williams (1992b) defined a class of TFRs called the reduced interference distributions (*RID*). The discrete-time Choi–Williams *RID* is:

$$CW-RID_x(n,k) = 2\sum_{\tau=-\infty}^{+\infty} w_N(\tau)e^{-j2\pi k\tau/N}\left[\sum_{\mu=(-\tau-|\tau|)/2}^{(-\tau+|\tau|)/2}\frac{1}{\sqrt{4\pi\tau^2/\sigma}}\exp\left(-\frac{(2\mu+\sigma)^2}{16\tau^2/\sigma}\right)x(n+\mu+\tau)x^*(n+\mu)\right]. \quad (4)$$

The Bessel distribution. Guo et al. (1994a) introduced the Bessel distribution (*BD*) based on the RID concept. The discrete-time *BD* is expressed as:

$$BD_x(n,k) = 2\sum_{\tau=-\infty}^{+\infty} w_N(\tau)e^{-j2\pi k\tau/N}\left[\sum_{\mu=(-\tau-2\alpha|\tau|)/2}^{(-\tau+2\alpha|\tau|)/2}\frac{2}{\pi\alpha|\tau|}\sqrt{1-\left(\frac{2\mu+\tau}{2\alpha\tau}\right)^2}\,x(n+\mu+\tau)x^*(n+\mu)\right], \quad (5)$$

where $\alpha > 0$ is a scaling factor. For all time-frequency methods described above (*SPEC, AR, CWD, CW-RID* and *BD*), the lag between each time window $w(\tau)$ or $w_N(\tau)$ was selected to 0.2 ms (time resolution).

The matching pursuit method (Gabor wavelet transformation). The matching pursuit method (Mallat and Zhang 1993) is based on a dictionary that contains a family of wavelet functions called time-frequency atoms. The decomposition of a signal is performed by projecting it over the function dictionary iteratively and by selecting the atoms or wavelets that can best match the local waveform of the signal. The matching pursuit method represents a discrete signal *x(n)* with *N* samples as:

$$x(n) = \sum_{i=0}^{+\infty}\alpha_i h_i(n), \quad (6)$$

with

$$h_i(n) = \beta_i g_i(n)u_i(n), \quad (7)$$

$$g_i(n) = g\left(\frac{n-p_i}{s_i}\right), \quad (8)$$

and

$$u_i(n) = \cos(2\pi k_i n/N + \theta_i). \quad (9)$$

In the above equations, α_i is the expansion coefficients that represent, when squared, the part of the signal energy associated with the atom $h_i(n)$. In eqn (7), the atom $h_i(n)$ is given by the product of the wavelet envelope function $g_i(n)$ with the sinusoid $u_i(n)$. The scale factors s_i are used to control the width of the envelope of $h_i(n)$, and p_i give the temporal positions of each atom. The parameters β_i are normalizing factors to keep the norm of $h_i(n)$ equal to 1. The parameters k_i and θ_i are the discrete frequency and phase of the cosine discrete function $u_i(n)$, respectively. In our application,

$$g_i(n) = 2^{1/4}e^{-\pi\left(\frac{n-p_i}{s_i}\right)^2} \quad (10)$$

is a Gabor function (Mallat and Zhang 1993).

Mallat and Zhang (1993) proposed to use the sum of the Wigner distributions of all the individual atoms composing a signal to represent its energy distribution in the time-frequency plane, which they called *MP*-based Wigner distribution. The *MP*-based Wigner distribution of *x(n)* in eqn (6) was represented as:

$$MP_x(n,k) = \sum_{i=1}^{L}\alpha_i^2\cdot W\left[h_i\left(\frac{n-p_i}{s_i}, 2\pi s_i(k-k_i)\right)\right], \quad (11)$$

where L is the number of atoms, α_i, p_i, s_i and k_i are the parameters of the ith time-frequency atom, and

$$W[h(n,k)] = 2e^{-2\pi(n^2+k^2)} \quad (12)$$

is the Wigner distribution of the atoms *h(n,k)*. In eqn (11), L and s_i are input parameters given to the model, whereas α_i, p_i, and k_i are output parameters characterizing each atom. To reduce the computational burden, the scale is generally limited to $s_i = 2^l$, where l is the octave of the scale s_i, which varies between 0 and $\log_2 N$. Hence, only the scales s_i that satisfy this relation and lie in [*1, N*] are selected from the dictionary. A predetermined maximum number of atoms is used to stop the iterative process. This reduces the computational burden and limits undesirable modeling of the background noise. It is important to note that the matching pursuit method finds the time-frequency atoms in a decreasing energy order. The higher-energy components of the signal are extracted first. Consequently, to track low-energy turbulent fluctuations, a high number of atoms may be necessary. For the current application, the position of each atom on the time scale was adjusted to allow a time resolution of 0.2 ms, which is similar to the value set for the other TFRs described above.

Simulation of Doppler signals under turbulent flow

The Doppler signal *s(n)*, sampled at 14 kHz, was simulated by a sum of sinusoids (Mo and Cobbold 1989), whose frequencies f_m subdivide the frequency range [0, $f_{\text{mmax}} + f_{\text{tmax}}$] in M bins of equal width Δf (see below the definition of the time-varying functions f_{mmax} and f_{tmax}). Because turbulence is an irregular eddying motion occurring about the mean velocities, a random frequency component $f_t(n)$ was used to generate *s(n)*.

$$s(n) = \sum_{m=1}^{M} \gamma_m(n)\cos[2\pi(f_m + f_t(n))n + \phi_m], \quad (13)$$

where

$$\gamma_m(n) = \sqrt{2S(n,k)\Delta f\, y_m} \quad (14)$$

is a Rayleigh distributed random variable, and

$$f_m = (m - 0.5)\Delta f. \quad (15)$$

The random phase ϕ_m is uniformly distributed between [0, 2π]; *S(n,k)* is the time-varying theoretical power spectral density function of the turbulence-free signal, defined over the range [0, f_{mmax}]; $\Delta f = f_{\text{mmax}}/M$ is an incremental frequency domain step; y_m is a χ^2 random variable with two degrees of freedom; and M is the number of sinusoids used to simulate the Doppler signal over the signal duration T. In the present study, a value of $M = 4185$ was chosen to respect the criterion defined by Mo and Cobbold (1989). Based on this criterion, the simulated Doppler signals were assumed to be Gaussian-distributed in amplitude.

The theoretical power spectral density of the pulsed-wave Doppler signal as a function of time, for a case without turbulence, is given by (Mo and Cobbold 1989):

$$S(n,k) = A(f_{m\max} - f_k)^2 \exp[-B(f_{m\max} - f_k)^2], \quad (16)$$

where f_{mmax}, A, and B are time-varying parameters representing the maximum frequency of the sinusoids f_m, the power scaling factor, and the bandwidth factor, respectively. The parameter f_k is the frequency corresponding to the spectral index k. In eqn (16), the greater the value of B, the narrower is the spectrum. The total power of the time-varying spectra *S(n,k)* were normalized to unity by varying the value of A.

In the current study, a Doppler signal of 293-ms duration was simulated containing positive frequencies during systole. The Doppler signal was not simulated during diastole because turbulence is not generated in the ascending aorta when the aortic valve is closed. The maximum time-varying frequency, f_{mmax}, was defined by:

$$f_{m\max}(n) = 3.5\sin(2\pi f_1 n) + 1 \quad (17)$$

where $f_1 = 1.79$ Hz, and f_{mmax} is in kHz. *A(n)* and *B(n)* in eqn (16) were chosen to values obtained by the procedure described by Guo et al. (1994b).

Because the maximum turbulence intensity under pulsatile flow usually occurs during the deceleration of the fluid (Shen 1961), the random frequencies f_t, which are Gaussian-distributed, were bounded between $\pm f_{\text{tmax}}(n)$ with the maximum occurring during late systole. The time varying parameter f_{tmax} was defined as a triangle, as represented by the dashed line in Fig. 1. The turbulent velocity fluctuations start at 84 ms, reach the maximum intensity at 168 ms, and decay to reach zero at 293 ms. Nygaard et. al. (1992) observed, for aortic mechanical heart valves implanted in humans, that the maximum turbulent Reynolds normal stress ($RNS = \rho\overline{u_n'^2}$), measured with hot-film anemometry, could reach 120 N/m^2, which corresponds to a velocity variance in the axial direction of the flow $\overline{u_n'^2}$, of 0.11 m^2/s^2 when considering a density of blood ρ at 1.093 g/cm^3. For a typical transmitted ultrasound frequency f_o of 5 MHz, a speed of sound c in blood at 1570 m/s, a maximum turbulent velocity fluctuation u_n' at 0.33 m/s and a Doppler angle θ of 60°, the Doppler frequency shift

$$f_d = \frac{2f_o u_n' \cos\theta}{c} = 1056 \text{ Hz}. \quad (18)$$

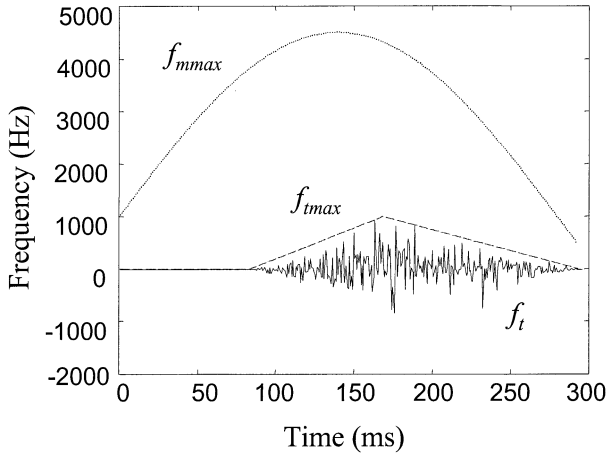

Fig. 1. Basic time-frequency functions of the parameters used to generate the Doppler signal *s(n)* of eqn (13). For each instant within the cycle, *M* sinusoids at frequencies f_m+f_t are summed to simulate *s(n)*. The maximum of f_m [*i.e.*, $f_{\mathrm{mmax}}(n)$] corresponds to the parabola (dotted line). The maximum of f_t [*i.e.*, $f_{\mathrm{tmax}}(n)$] is given by the dashed triangular curve. The solid line represents an example of the Gaussian frequency fluctuations, f_t, simulating flow turbulence.

In the present study, the maximum frequency value f_{tmax} at 168 ms was chosen to be 1 kHz (0.314 m/s) for most evaluations. A higher maximum turbulence intensity of 2 kHz (0.628 m/s) was also used to test the stability of the TFR methods to an increase in turbulence level. Fig. 1 summarizes the basic time-frequency functions of the parameters used to generate the Doppler signal *s(n)* with eqn (13). Fig. 2 shows examples of simulated time-varying Doppler spectra without turbulence (*i.e.*, $f_t = 0$ Hz), and with a maximum turbulence intensity bounded between $f_{\mathrm{tmax}}(n) = \pm 1$ kHz ($\pm$ 0.314 m/s). Because the maximum frequency of the function $f_{\mathrm{mmax}}(n)$ defined by eqn (17) was 4.5 kHz, the simulated conditions can correspond to a maximum blood flow velocity in the ascending aorta of 1.4 m/s, when considering the Doppler parameters defined above. In this study, although both the in-phase and quadrature components of the Doppler signal *s(n)* were generated, only the in-phase signal was used. This choice is justified by the fact that the statistical characteristics of the in-phase and quadrature signals are the same, and that reverse flow was absent from the simulations.

Optimization of the parameters affecting the performance of the TFR methods

Table 1 presents the range of parameters tested to optimize the performance of each TFR technique. The parameters investigated were the window type, window length, model order, parameter σ, parameter α, the octave parameter *l*, and the maximum number of atoms *L*.

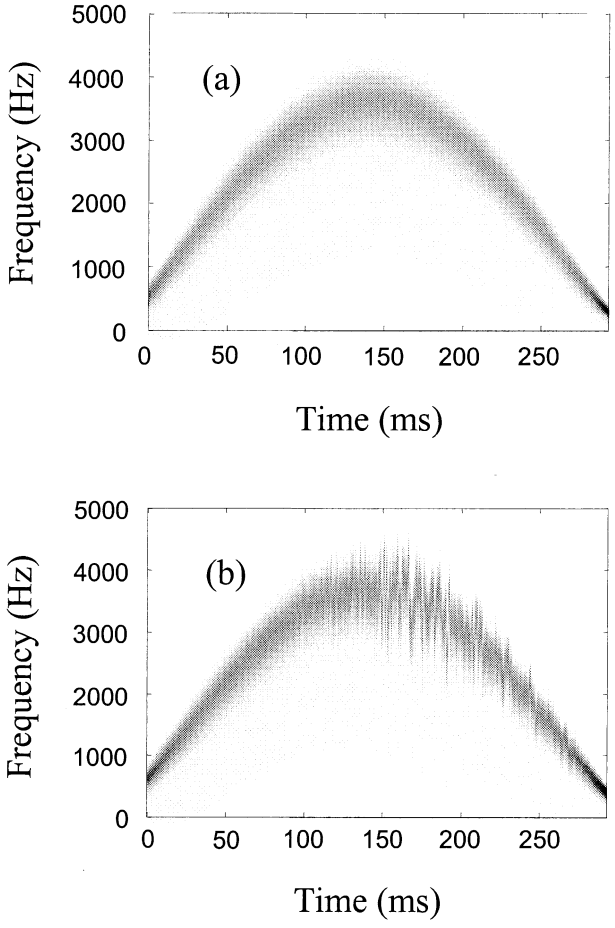

Fig. 2. Examples of simulated Doppler TFR, *S(n,k)*, (a) without turbulence and (b) with maximum turbulent frequency fluctuations bounded between $f_{\mathrm{tmax}}(n) = \pm 1$ kHz ($\pm$ 0.314 m/s).

The types of window tested are rectangular, hanning, hamming, and sine-cosine. For the sine-cosine window, the first 10% of the samples were weighted by the sine function (computed between 0 and 90°), and the last 10% by the cosine also defined between 0 and 90°.

Assessment of the performance of the TFR methods

To track the turbulent velocity fluctuations, the instantaneous mean frequency waveform was estimated from the Doppler power spectra according to the following equation:

$$\hat{f}_{mean}(n) = \frac{\sum_{k=K_{\mathrm{bwlow}}}^{K_{\mathrm{bwhigh}}} f_k \hat{S}[n,k]}{\sum_{k=K_{\mathrm{bwlow}}}^{K_{\mathrm{bwhigh}}} \hat{S}[n,k]}, \tag{19}$$

where K_{bwlow} and K_{bwhigh} are the samples corresponding to the lower and higher frequencies of the -5-dB band-

Table 1. Parameters of the time-frequency representation techniques and their ranges of values

Time-frequency technique	Window type	Window length (ms)	Other parameters
SPEC	rectangular, hanning, hamming, sine-cosine	1, 2, 5, 10	–
AR	rectangular, hanning, hamming, sine-cosine	1, 2, 5, 10	model order = 8, 10, 12, 14, 16
CWD	w_N = rectangular, sine-cosine	w_N = 1, 2, 5, 10	σ = 0.01, 0.05, 0.1, 0.2
	w_M = rectangular	w_M = 1, 2, 5, 10	–
CW-RID	w_N = rectangular, sine-cosine	w_N = 1, 2, 5, 10	σ = 0.01, 0.05, 0.1, 0.2
BD	w_N = rectangular, sine-cosine	w_N = 1, 2, 5, 10	α = 1, 2, 5, 10, 16
MP	–		Octave parameter (l): 7, 8, 9, 10, 11 Maximum number of atoms (L): 100, 150, 300, 500, 1000

width of the dominant frequency peak, f_k is the frequency corresponding to the spectral index k, and $\hat{S}$ represents the TFR of each method tested on the Doppler signal $s(n)$. To assess the performance of each method, $\hat{f}_{\text{mean}}$ was compared to the theoretical mean frequency waveform, f_{mean}, evaluated from the theoretical time-varying power spectral density. More specifically, f_{mean} was computed as:

$$f_{\text{mean}}(n) = f_{m\,\max}(n) + f_t(n) - \frac{2}{\sqrt{\pi B(n)}}, \qquad (20)$$

where n is the discrete time, $f_{\text{mmax}}(n)$ is defined in eqn (17), $f_t(n)$ is the Gaussian-distributed random frequency simulating turbulence, and $B(n)$ is the bandwidth factor. As described by Guo et al. (1994b), the theoretical computation of $f_{\text{mean}}(n)$ can be found analytically. Figure 3 shows the theoretical mean frequency waveform $f_{\text{mean}}(n)$ for no turbulence (*i.e.*, $f_t(n) = 0$) and a case with a maximum turbulent frequency fluctuation $f_{\text{tmax}}(n) = \pm 1$ kHz (± 0.314 m/s).

Three procedures were used to test the accuracy of each TFR method to track turbulent velocity fluctuations. It is important to remember that, in the absence of turbulence, the fluctuations of the Doppler mean velocities are attributed to the variance of the spectral estimator.

Procedure 1. The accuracy of each method for measuring the absolute turbulent frequency fluctuations was determined by computing the following difference equation:

$$\text{Mean\_Abs\_Freq\_Dif} = \frac{1}{N_c} \sum_{n=N_1}^{N_2} \{|\hat{f}_t(n)| - |f_t(n)|\}, \qquad (21)$$

where N_c is the number of samples between the time indexes $N_1 = 84$ ms and $N_2 = 293$ ms (period over which turbulence was simulated), $\hat{f}_t(n)$ is the zero-mean turbulent frequency fluctuations measured with each TFR method, and $f_t(n)$ corresponds to the simulated turbulent Doppler signal fluctuations (Fig. 1). The index Mean_Abs_Freq_Dif, expressed in Hz, allows assessment of the accuracy of the frequency fluctuations, independently of the phase of the signal (because absolute frequencies are computed). A value of zero for this index

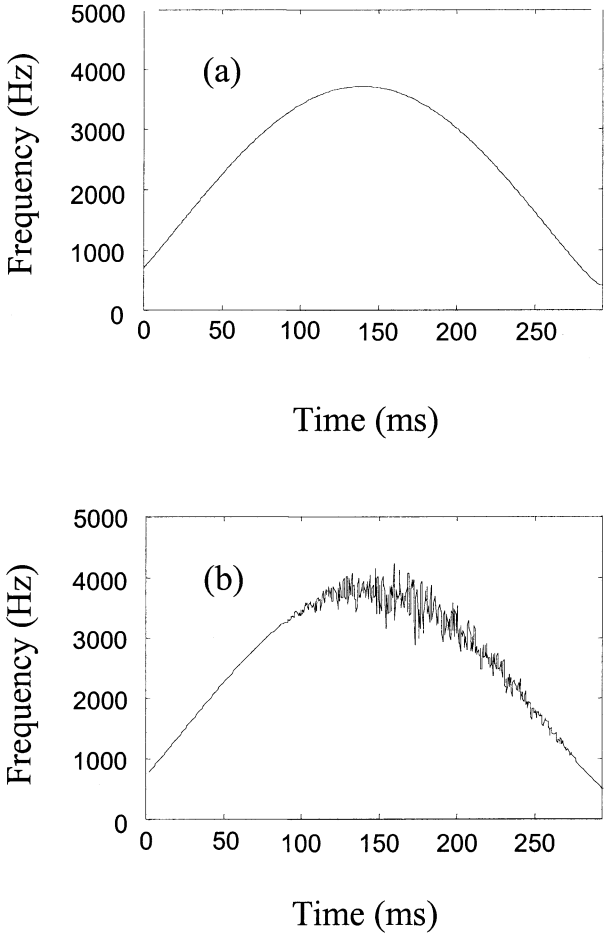

Fig. 3. Theoretical mean frequency waveform $f_{\text{mean}}(n)$ for (a) no turbulence and (b) a case with maximum turbulent frequency fluctuations $f_{\text{tmax}}(n) = \pm 1$ kHz ($\pm$ 0.314 m/s).

means a good accuracy of the TFR technique to track the magnitude of the Doppler turbulent fluctuations; a value above zero indicates an overestimation, whereas a value below zero means an underestimation of the magnitude of the fluctuations.

Procedure 2. By definition, the intensity of turbulence, in m/s, is given by the r.m.s. of the turbulent velocity fluctuations. The turbulence intensity was computed, between $N_1 = 0$ ms and $N_2 = 293$ ms, with the following equation:

$$\text{Turb\_Int}\,(n) = \sqrt{\frac{1}{N_{\text{cycle}}}\sum_{m=1}^{N_{\text{cycle}}}\hat{v}_t(n,m)^2}, \qquad (22)$$

where n is the time increment, m is the cardiac cycle considered, $N_{\text{cycle}} = 30$ is the number of cycles simulated, and $\hat{v}_t$ is the velocity of the turbulent fluctuations obtained by converting the frequency fluctuations $\hat{f}_t(n)$ into velocity fluctuations $\hat{v}_t(n)$ by applying the classical Doppler equation. For comparison, eqn (22) was also computed by using the theoretical turbulent fluctuations $f_t(n)$.

Procedure 3. Turbulent blood flow produces a broad range of eddy sizes, each having a different velocity fluctuation when moving in the mainstream at a finite mean velocity. The Kolmogorov power spectrum (Hinze 1975; Nygaard 1994), which can be displayed in the form of a log-log plot of the turbulent power as a function of frequency, is commonly used to characterize the size of turbulent eddies (scale of turbulence). Typically, the Kolmogorov spectrum is computed from the turbulent fluctuations $\hat{f}_t(n)$ or $f_t(n)$. The low frequencies of the Kolmogorov spectrum correspond to large permanent eddies (typically frequencies < 20 Hz), whereas microscale turbulent motions are in the upper frequency range of the spectrum (typically > 1000 Hz).

As reviewed by Hinze (1975), the rate of increase or decay of the spectral density as a function of frequency determines the proportion of each eddy size in the volume of interest (large permanent eddies, energy-containing eddies, Kolmogorov inertial subrange, and microscale turbulent motions). For isotropic turbulence, the slopes of the log-log spectrum, in decades of power per decades of frequency, have been theoretically derived for each of these frequency ranges. Values are between 4 and 1 for the low-frequency permanent eddies, between 1 and $-5/3$ for energy-containing eddies (Von Kármán's power law), $-5/3$ for the inertial subrange (Kolmogorov's power law), and -7 for microscale eddies (Heisenberg's power law). These slopes were obtained for high Reynolds numbers where viscosity effects are negligible

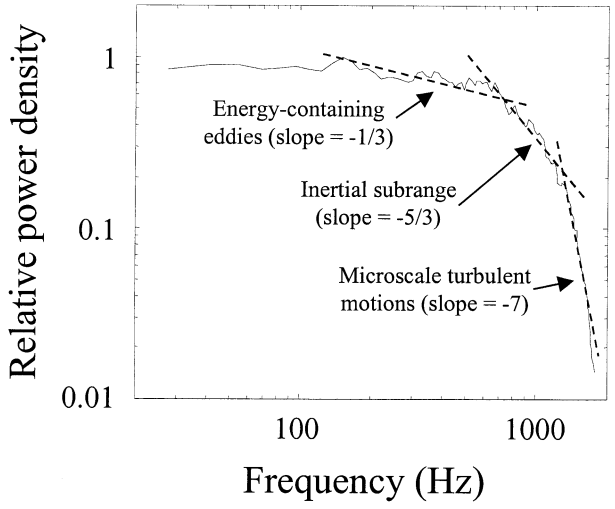

Fig. 4. Kolmogorov power spectrum averaged over 30 flow cycles for turbulent frequency fluctuations $f_t(n)$ bounded between $f_{t\max}(n) = \pm 1$ kHz (± 0.314 m/s). For each flow cycle, the mean spectrum was computed between 84 and 293 ms by applying the Welch spectral method (Welch 1967) over 50-ms nonoverlapping rectangular windows. The theoretical slopes for the different frequency ranges considered, in decades of power per decades of frequency, are indicated on the graph (Hinze 1975). The -10-dB bandwidth of this spectrum (parameter $BW_{-10\text{ dB}}$ of eqn (23) is 1449 Hz.

(Hinze 1975). Figure 4, described later, shows the simulated Kolmogorov spectrum used in this study.

Computing the following equation assessed the accuracy of each TFR method to track the whole range of eddy sizes:

$$BW\_\text{Dif} = BW_{-10\text{ dB}}(K[\hat{f}_t] - K[f_t]), \qquad (23)$$

where BW_Dif, in Hz, is the difference of the maximum frequencies that correspond to the bandwidth at -10 dB ($BW_{-10\text{ dB}}$) of the Kolmogorov spectrum of the estimated fluctuations obtained from each TFR method, $K[\hat{f}_t]$, and of the simulated frequency fluctuations, $K[f_t]$. To compute the Kolmogorov spectrum, nonoverlapping 50-ms rectangular windows were applied, between $N_1 = 84$ ms and $N_2 = 293$ ms, to the signals $\hat{f}_t(n)$ and $f_t(n)$ sampled at a frequency of 5 kHz (the sampling frequency corresponds to the time resolution of the TFR methods, which is 0.2 ms). A power spectrum was evaluated for each 50-ms window by using the discrete Fourier transform and a reliable estimate of the Kolmogorov spectrum was obtained by averaging the power spectra over 1 or 30 cardiac cycles (Welch 1967). Only 1 cycle was considered when determining the optimal parameters of each TFR method, whereas 30 cycles were used when performing the final comparison of the TFR techniques.

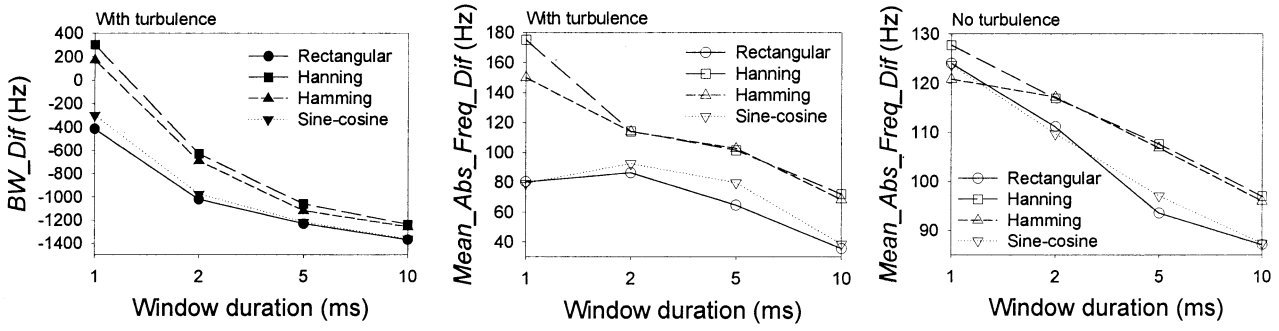

Fig. 5. Optimization of the spectral parameters for the spectrogram. Parameters *BW*_Dif, eqn (23), and Mean_Abs_Freq_Dif, eqn (21), are plotted as a function of the window duration for simulations with and without turbulence. In the case of turbulence, the maximum frequency fluctuations $f_{tmax}(n) = \pm 1$ kHz ($\pm$ 0.314 m/s). The legend gives the window type that corresponds to each curve.

Tested conditions. The best parameters of each TFR method were selected from one typical flow cycle by minimizing *BW*_Dif and Mean_Abs_Freq_Dif. The performance assessment was determined for the cases of no turbulence, and for a maximum turbulent frequency fluctuation $f_{tmax}(n) = \pm 1$ kHz ($\pm$ 0.314 m/s). After having obtained the best set of parameters for each TFR technique, comparison of the methods was performed over 30 independent simulated cardiac cycles without turbulence, and with maximum turbulent fluctuations $f_{tmax}(n) = \pm 1$ kHz ($\pm$ 0.314 m/s) and ± 2 kHz ($\pm$ 0.628 m/s). The selection of the best method was based on a statistical analysis of variance on the parameters *BW*_Dif and Mean_Abs_Freq_Dif. The turbulence intensity Turb_Int*(n)* and the Kolmogorov spectrum were computed for the best methods.

RESULTS

The Kolmogorov spectrum of $f_t(n)$ was evaluated over 30 flow cycles generated with independent random sequences. Figure 4 presents the power spectrum for a maximum turbulent frequency fluctuation $f_{tmax}(n)$ of ± 1 kHz ($\pm$ 0.314 m/s). Because only the magnitude of the fluctuations changed for simulations with $f_{tmax}(n) = \pm 2$ kHz, the Kolmogorov mean spectrum for this case is very similar. According to the mean spectrum of Fig. 4, the whole scale of turbulent fluctuations was simulated (large vortex to small eddy).

Optimization of the parameters for each TFR method

The criteria allowing selection of the best set of parameters are the following: 1. The TFR method should be able to track rapid turbulent fluctuations. This means that the bandwidth at -10 dB of the Kolmogorov spectrum should be as close as possible to that of the simulated fluctuations (*BW*_Dif should tend toward 0 Hz). 2. The TFR method should be able to estimate the magnitude of the absolute frequency fluctuations. This criterion means that Mean_Abs_Freq_Dif should converge toward 0 Hz for the simulations performed with turbulence. Finally, 3. the variance of the TFR algorithm should be minimum. In other words, Mean_Abs_Freq_Dif also should tend toward 0 Hz for the simulations performed without turbulence.

As shown in Fig. 5, few differences were found between the rectangular and sine-cosine windows, and between the hanning and hamming windows for the spectrogram. When there was turbulence, the Kolmogorov spectrum was better modeled when the window length was reduced from 10 to 1 ms, for all window types. On the other hand, the parameter Mean_Abs_Freq_Dif was generally reduced as the window length was increased for both turbulent and laminar flows. According to the selection criteria defined above, the 1-ms hamming or sine-cosine windows are good selections to model the Kolmogorov spectrum. Both the 10-ms rectangular and sine-cosine windows minimized the parameter Mean_Abs_Freq_Dif for turbulent and laminar flows within the range of window durations considered.

Although several model orders (8 to 16) were tested for autoregressive modeling, this parameter had no significant effect on the results. Thus, the data in Fig. 6 are presented for a fixed model order of 8. The variations of *BW*_Dif and Mean_Abs_Freq_Dif as a function of the window length and type were very similar to those obtained with the spectrogram. However, for no turbulence, the variance of the *AR* estimator was slightly larger than the spectrogram. According to Fig. 6, the 1-ms sine-cosine window is the best selection to minimize the bias of *BW*_Dif. On the

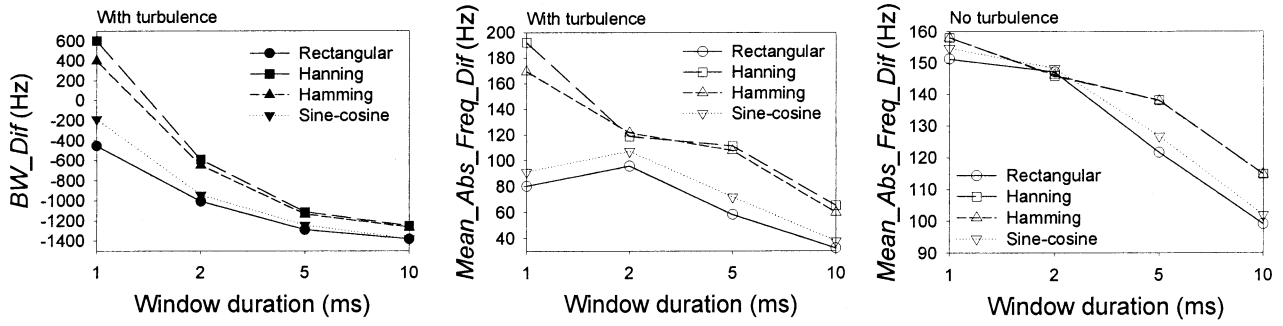

Fig. 6. Optimization of the spectral parameters for autoregressive modeling (model order = 8). Parameters *BW*_Dif, eqn (23), and Mean_Abs_Freq_Dif, eqn (21), are plotted as a function of the window duration for simulations with and without turbulence. In the case of turbulence, the maximum frequency fluctuations $f_{tmax}(n) = \pm 1$ kHz ($\pm$ 0.314 m/s). The legend gives the window type that corresponds to each curve.

other hand, the 10-ms rectangular window provided the best estimate of Mean_Abs_Freq_Dif for both turbulent and laminar flows.

The results obtained with the Choi–Williams distribution were better when using a rectangular window instead of the sine-cosine function for w_N (results not shown). Effectively, for any given window duration w_M and w_N, and any values of the parameter σ, the bandwidth of the Kolmogorov spectrum was always more severely underestimated with the sine-cosine window w_N. On the other hand, Mean_Abs_Freq_Dif was not significantly affected by the window type w_N. The effect of varying the length of w_N between 1 and 10 ms was as follows (results not shown): changing the length had very little effect on the Kolmogorov spectral bandwidth; Mean_Abs_Freq_Dif was almost unaffected by this parameter for the case of turbulence; and Mean_Abs_Freq_Dif slightly decreased as the window length w_N was increased when there was no turbulence. According to these observations, the results in Fig. 7 are presented for w_N being a 10-ms rectangular window. As seen on this figure, the bandwidth of the Kolmogorov spectrum increased (*BW*_Dif converged toward 0 Hz) as the window duration w_M was reduced, and that was observed for any values of the parameter σ. The tendency for the effect of w_M on Mean_Abs_Freq_Dif is the opposite, reducing the window length increased the error in the estimate of the absolute turbulent fluctuations and variance of the TFR estimator. According to Fig. 7, the best set of parameters to reduce *BW*_Dif is w_N = 10-ms rectangular window, w_M = 1-ms rectangular window, and $\sigma = 0.1$. For Mean_Abs_Freq_Dif, the best parameters are w_N and w_M = 10-ms rectangular windows, and $\sigma = 0.01$ for both turbulent and laminar flows.

Figure 8 presents the results obtained with the *CW-RID* method and w_N = a sine-cosine window. The results for the rectangular window are not given because the values of Mean_Abs_Freq_Dif were at least 2 times

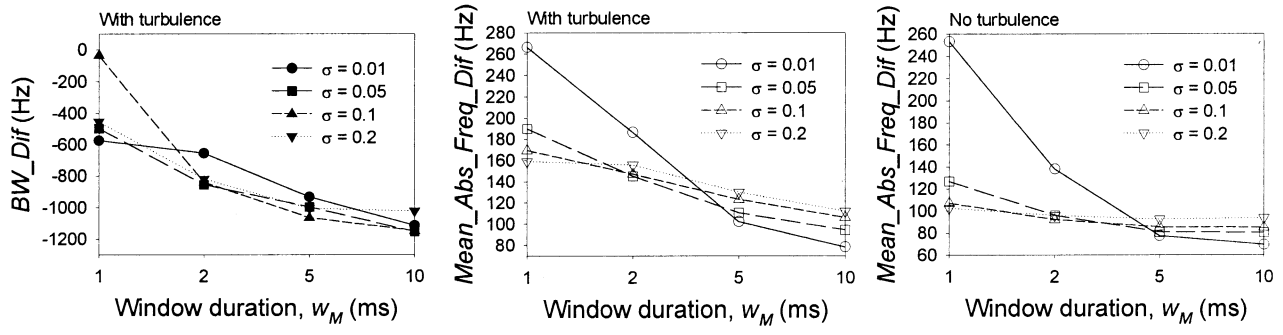

Fig. 7. Optimization of the spectral parameters for the Choi–Williams distribution (w_N = 10-ms rectangular window, w_M = rectangular). Parameters *BW*_Dif, eqn (23), and Mean_Abs_Freq_Dif, eqn (21), are plotted as a function of the window duration w_M for simulations with and without turbulence. In the case of turbulence, the maximum frequency fluctuations $f_{tmax}(n) = \pm 1$ kHz ($\pm$ 0.314 m/s). The legend gives the value of the parameter σ (controls of the auto-term resolution for cross-term suppression) that corresponds to each curve.

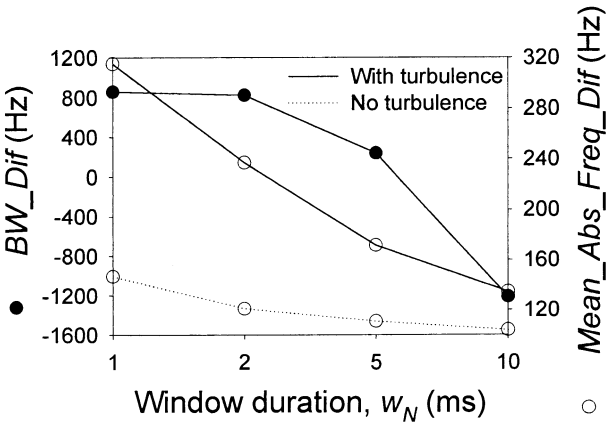

Fig. 8. Optimization of the spectral parameters for the Choi–Williams reduced interference distribution (w_N = sine-cosine and σ = 0.1). Parameters *BW*_Dif, eqn (23), and Mean_Abs_Freq_Dif, eqn (21), are plotted as a function of the window duration w_N for simulations with and without turbulence. In the case of turbulence, the maximum frequency fluctuations $f_{tmax}(n) = \pm$ 1 kHz ($\pm$ 0.314 m/s).

larger for any given values of the window length and parameter σ. With this TFR method, σ had no effect on *BW*_Dif and Mean_Abs_Freq_Dif (the variance of the results was within $\pm$ 1 Hz), consequently the results of Fig. 8 are presented for σ = 0.1 only. The optimal window duration for this TFR was 5 ms when modeling the Kolmogorov spectrum. To estimate the absolute turbulent fluctuations and to minimize the variance in the absence of turbulence, the 10-ms window is better.

The results for the Bessel distribution are presented in Fig. 9. Both the sine-cosine and rectangular windows w_N provided similar satisfactorily results. Generally, Mean_Abs_Freq_Dif was slightly smaller when using the sine-cosine window (results not shown). On the other hand, the bandwidth of the Kolmogorov spectrum was better estimated with the rectangular window. Consequently, this window was used for Fig. 9. According to this figure, the best compromise for *BW*_Dif is obtained with the 2-ms window and α = 2. To estimate Mean_Abs_Freq_Dif, the best results were obtained with the 10-ms rectangular window and α = 16.

As seen in Fig. 10, the matching pursuit did not provide satisfactory results to estimate the Kolmogorov bandwidth. However, by properly selecting the number of atoms and the octave parameter, similar results to the other TFR techniques could be obtained for Mean_Abs_Freq_Dif. The best parameters to estimate *BW*_Dif and Mean_Abs_Freq_Dif are the octave parameter l = 10 and the number of atoms L of 150.

*Selection of the best techniques to model BW*_Dif *and* Mean_Abs_Freq_Dif

According to the above results, more than one TFR technique and more than one set of parameters can be selected to track turbulent motions. For a given technique, it is also clear that different parameters must be used to optimally determine the Kolmogorov spectrum, minimize the variance of the estimator, and measure the absolute turbulent frequency fluctuations. To help compare each technique, Table 2 shows *BW*_Dif computed over 30 flow cycles for the optimal parameters selected earlier. The first three columns present results for no turbulence, and turbulent fluctuations $f_{tmax}(n) = \pm$ 1 kHz ($\pm$ 0.314 m/s) and $\pm$ 2 kHz ($\pm$ 0.628 m/s), respectively. The absolute values of *BW*_Dif also were computed for each column and averaged to give the mean bias of each technique (the bias is given in the fourth column and it is named the mean of the absolute *BW*_Dif; absolute values were used because *BW*_Dif could be either positive or negative). To determine the best technique, an analysis of variance (one-way ANOVA, SigmaStat statistical software, SPSS, San Rafael, CA, version 2.03) was per-

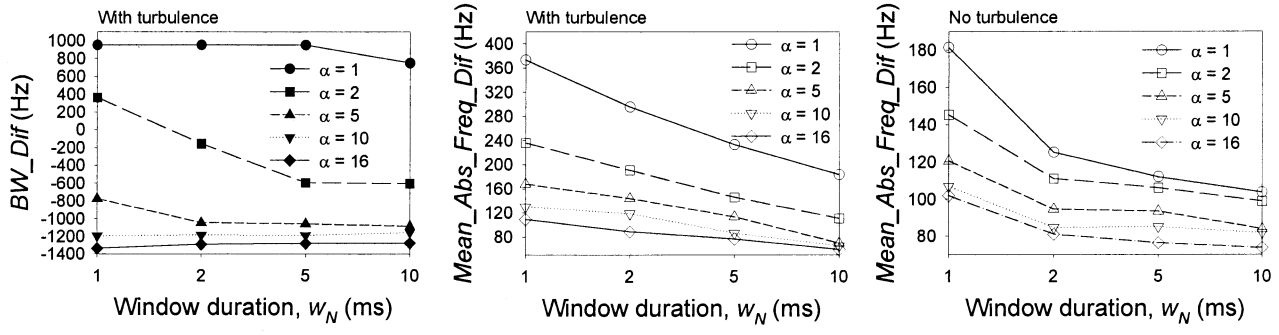

Fig. 9. Optimization of the spectral parameters for the Bessel distribution (w_N = rectangular). Parameters *BW*_Dif, eqn (23), and Mean_Abs_Freq_Dif, eqn (21), are plotted as a function of the window duration w_N for simulations with and without turbulence. In the case of turbulence, the maximum frequency fluctuations $f_{tmax}(n) = \pm$ 1 kHz ($\pm$ 0.314 m/s). The legend gives the value of the parameter α (scaling factor) that corresponds to each curve.

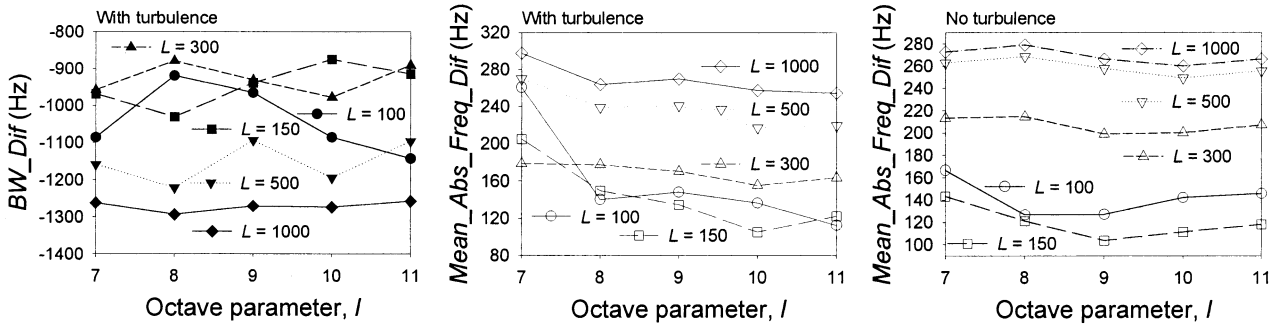

Fig. 10. Optimization of the spectral parameters for the matching pursuit method. Parameters *BW*_Dif, eqn (23), and Mean_Abs_Freq_Dif, eqn (21), are plotted as a function of the octave parameter *l* for simulations with and without turbulence. In the case of turbulence, the maximum frequency fluctuations $f_{tmax}(n) = \pm 1$ kHz ($\pm$ 0.314 m/s). The legend gives the number of atoms (L) used for the computation of the TFR that correspond to each curve.

formed on the means of the absolute *BW*_Dif. From Table 2, the Bessel distribution with $w_N = 2$ ms rectangular windows and $\alpha = 2$ provided the smallest bias of the Kolmogorov mean spectra with a value for the bandwidth at -10 dB of 355 $\pm$ 139 Hz. Although the biases for the spectrogram, *AR* modeling, and the *CW-RID* distribution were higher, these values were not statistically different from those obtained with the Bessel distribution.

In theory, *BW*_Dif should be 0 Hz when there is no turbulence. As noted in the first column of Table 2, the variance of all TFR estimators produced fluctuations characterized by finite bandwidths. Among the best four algorithms (*SPEC, AR, CW-RID* and *BD*), the frequency of these fluctuations was minimum for the Bessel distribution (*BW*_Dif = 354 $\pm$ 51 Hz). In the absence of turbulence, the worse results (fastest fluctuations that could be interpreted as fast turbulent eddies) were obtained with the spectrogram. On the other hand, this technique provided the best estimate of the Kolmogorov mean spectrum when there was turbulence (*BW*_Dif = 85 $\pm$ 108 Hz and 50 $\pm$ 149 Hz for $f_{tmax}(n) = \pm 1$ and $\pm$ 2 kHz, respectively). According to this discussion, the Bessel distribution is recommended if one wants to respect the criterion of the Kolmogorov spectral bandwidth.

Table 3 shows the best techniques to minimize the variance in the absence of turbulence, and to estimate the absolute turbulent fluctuations (parameter Mean_Abs_Freq_Dif). The fourth column gives the mean of the absolute values of Mean_Abs_Freq_Dif computed over the first three columns. Based on an analysis of variance, the mean of the absolute Mean_Abs_Freq_Dif was optimum for the spectrogram, *AR* modeling, the Choi–Williams distribution, and the Bessel distribution. All four methods provided mean values close to 60 Hz. In the absence of turbulence, the variance of the TFR estimators was minimum for the Choi–Williams distribution (Mean_Abs_Freq_Dif = 79 $\pm$ 10 Hz). For all methods, the magnitude of the

Table 2. Optimal parameters to model the Kolmogorov spectral bandwidth (parameter *BW*_Dif) for each TFR technique

Time-frequency technique	No turbulence (Hz)	Frequency fluctuations (Hz) ($f_{tmax}(n) = \pm 1$ kHz)	Frequency fluctuations (Hz) ($f_{tmax}(n) = \pm 2$ kHz)	Mean of the absolute *BW*_Dif (Hz)	*p*
SPEC, 1 ms hamming	1059 $\pm$ 263	85 $\pm$ 108	50 $\pm$ 149	434 $\pm$ 94	–
AR, 1 ms sine-cosine; model order = 8	699 $\pm$ 200	-117 ± 281	-178 ± 308	430 $\pm$ 102	–
CWD, $w_N = 10$ ms rect.; $w_M = 1$ ms rect.; $\sigma = 0.1$	750 $\pm$ 176	-566 ± 206	-614 ± 136	644 $\pm$ 72	*
CW-RID, $w_N = 5$ ms sine-cosine; $\sigma = 0.1$	414 $\pm$ 71	-342 ± 422	-436 ± 342	441 $\pm$ 139	–
BD, $w_N = 2$ ms rect.; $\alpha = 2$	354 $\pm$ 51	-193 ± 371	-255 ± 364	355 $\pm$ 139	–
MP, $l = 10$; $L = 150$	348 $\pm$ 57	-974 ± 112	-962 ± 106	762 $\pm$ 48	*

The results are presented for no turbulence and for maximum frequency fluctuations of $\pm$ 1 kHz ($\pm$ 0.314 m/s) and $\pm$ 2 kHz ($\pm$ 0.628 m/s). The absolute values of *BW*_Dif were averaged over the data of the first three columns, and results are presented in the fourth column (mean of the absolute *BW*_Dif). All results were averaged over 30 flow cycles (mean $\pm$ one SD). *SPEC, AR, CW-RID* and *BD* represent the best techniques as confirmed by an analysis of variance on the means of the absolute *BW*_Dif.

See text for the definition of the terms; *$p < 0.001$.

Table 3. Optimal parameters to minimize the variance of the spectral estimator and to estimate the absolute turbulent frequency fluctuations (parameter Mean_Abs_Freq_Dif) for each TFR technique

Time-frequency technique	No turbulence (Hz)	Frequency fluctuations (Hz) ($f_{max}(n) = \pm$ 1 kHz)	Frequency fluctuations (Hz) ($f_{tmax}(n) = \pm$ 2kHz)	Mean of the absolute Mean_Abs_Freq_Dif (Hz)	p
SPEC, 10-ms sine-cosine	95 ± 14	65 ± 18	−21 ± 21	61 ± 9	
AR, 10-ms rectangular; model order = 8	95 ± 12	62 ± 16	−26 ± 21	62 ± 8	
CWD, w_N = 10 ms rect.; w_M = 10 ms rect.; σ = 0.01	79 ± 10	86 ± 18	5 ± 24	62 ± 8	
CW-RID, w_N = 10 ms sine-cos; σ = 0.1	116 ± 11	135 ± 13	51 ± 17	101 ± 9	*
BD, w_N = 10 ms rect.; α = 16	85 ± 15	73 ± 21	−11 ± 28	61 ± 9	
MP, l = 10; L = 150	116 ± 19	165 ± 27	98 ± 46	126 ± 20	*

The results are presented for no turbulence and for maximum turbulent frequency fluctuations of ± 1 kHz (± 0.314 m/s) and ± 2 kHz (± 0.628 m/s). The absolute values of Mean_Abs_Freq_Dif were averaged over the data of the first three columns, and results are presented in the fourth column (mean of the absolute Mean_Abs_Freq_Dif). All results were averaged over 30 flow cycles (mean ± one SD). *SPEC*, *AR*, *CWD*, and *BD* represent the best techniques, as confirmed by an analysis of variance on the means of the absolute Mean_Abs_Freq_Dif.

See text for the definition of the terms; *$p < 0.001$.

turbulent frequency fluctuations was overestimated for the smallest fluctuations (± 1 kHz), whereas it was underestimated or closer to the true simulated value for the highest value of ± 2 kHz.

Turbulent time-intensity variations and Kolmogorov mean spectrum

According to Tables 2 and 3, three TFR methods, each with a different set of parameters, can optimize the Kolmogorov mean spectrum, the variance of the estimator, and the absolute turbulent frequency fluctuations (*SPEC*, *AR* and *BD*). Arbitrarily, this section shows results obtained with the spectrogram and the Bessel distribution. Figure 11 presents Turb_Int*(n)*, in m/s, for the case of no turbulence, and a maximum turbulent fluctuation $f_{tmax}(n) = \pm$ 1 kHz. The theoretical time-varying values of this parameter are presented for comparison. As expected from Table 3, both techniques estimated velocity fluctuations in the absence of turbulence. The mean intensity was on the order of 0.04 m/s for both TFR methods. When computed as a relative index :

$$1/N \sum_{n=0}^{N} \hat{f}_t(n) \times 100/f_{mean}(n), \qquad (24)$$

the coefficient of variation was 12.4% for *SPEC* and 8.0% for *BD*. For *AR*, the coefficient of variation was 14.5% (results not shown). The intensity of the fluctuations was overestimated when compared to the fluctuations measured from the theoretical TFR, for the case of turbulence. Neither the spectrogram, the Bessel distribution nor any other methods (*AR, CWD, CW-RID, MP*) could accurately estimate the triangular shape of the turbulent intensity. At the peak of the simulated turbulent

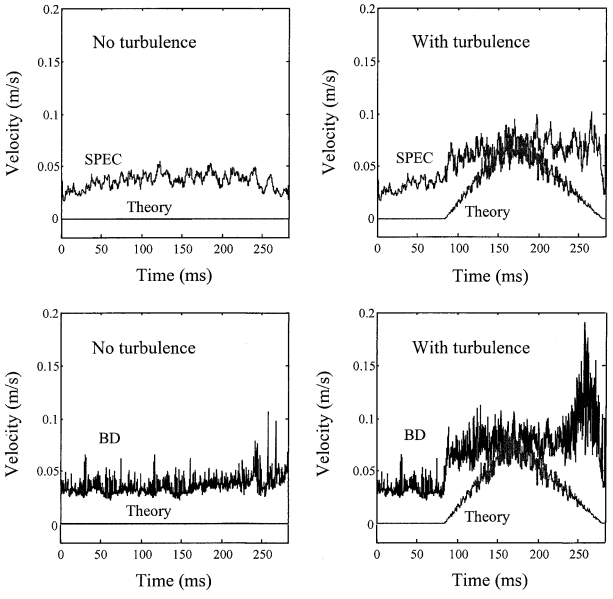

Fig. 11. Intensity of the velocity fluctuations in m/s (*i.e.*, parameter Turb_Int, eqn (22)), as a function of the timing within the flow cycle for measurements performed with the spectrogram (*SPEC*) and the Bessel distribution (*BD*). The parameters used were 10-ms sine-cosine windows for *SPEC*, and w_N = 10-ms rectangular windows and α = 16 for *BD*. A total of 30 flow cycles were used to compute the parameter Turb_Int*(n)*. The results are given for no turbulence, and maximum turbulent frequency fluctuations $f_{tmax}(n) = \pm$ 1 kHz (± 0.314 m/s). The expected simulated velocity fluctuations are indicated on the figure (theory). Note that the maximum of Turb_Int is about one third of $f_{tmax}(n)$, which is 0.314 m/s. By definition (eqn (22)), Turb_Int is the r.m.s. of the simulated velocity fluctuations, which is equivalent to the standard deviation (SD). Because 99.7% of the values are within the mean ± 3 SD for a Gaussian statistical distribution, this explains the smaller values noted in this figure.

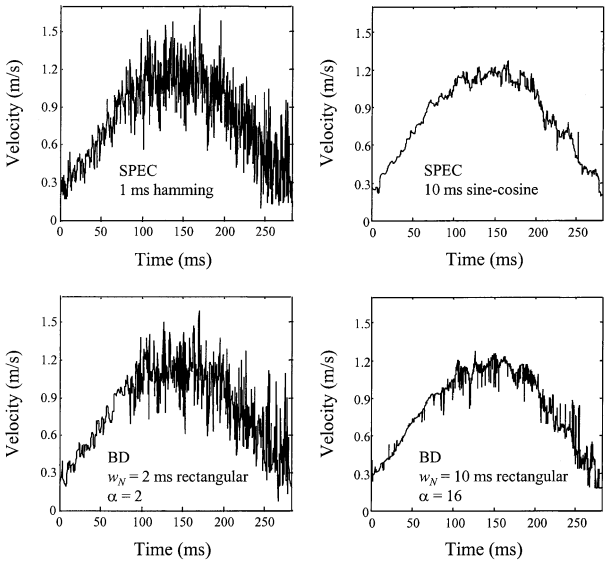

Fig. 12. Typical mean velocity waveforms over one flow cycle obtained with the spectrogram (*SPEC*) and the Bessel distribution (*BD*), for maximum turbulent frequency fluctuations $f_{t\text{-}max}(n) = \pm 1$ kHz ($\pm$ 0.314 m/s). Optimally, these waveforms should depict the theoretical variations noted in Fig. 3b. The parameters used for each spectral method are indicated on the figure. The left panels represent the mean waveforms for parameters optimized to model the Kolmogorov spectrum, whereas the right panels give the results for parameters selected to reduce the velocity variance and to measure the magnitude of the turbulent frequency fluctuations.

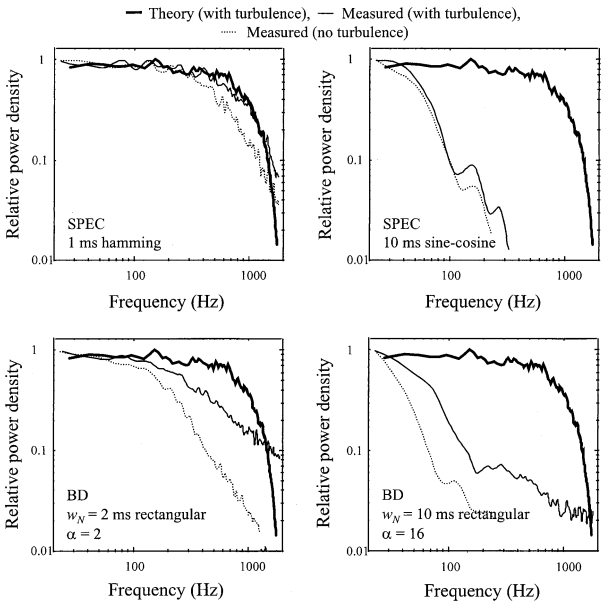

Fig. 13. Kolmogorov power spectrum averaged over 30 flow cycles for turbulent frequency fluctuations bounded between $f_{tmax}(n) = \pm 1$ kHz ($\pm$ 0.314 m/s), and for the case of no turbulence. The spectrum obtained from the simulations is also presented for comparison (theory). The parameters used for the spectrogram (*SPEC*) and the Bessel distribution (*BD*) are indicated on the figure. The left panels present the spectra for parameters optimized to track the velocity fluctuations, whereas the right panels give the results for parameters selected to reduce the velocity variance and to measure the magnitude of the turbulent frequency fluctuations.

intensity, the bias of both *SPEC* and *BD* methods was below 0.01 m/s.

Figure 12 presents, for one typical flow cycle, the mean velocity as a function of time for a maximum turbulent fluctuation of $\pm$ 1 kHz ($\pm$ 0.314 m/s). The left panels show the mean waveforms for parameters optimized to estimate the Kolmogorov spectrum, whereas the right panels give the results for parameters selected to reduce the velocity variance and to measure the absolute turbulent frequency fluctuations. The Kolmogorov power spectra corresponding to the cases of Fig. 12 are shown in Fig. 13. As noted earlier, the spectrogram with 1-ms hamming windows is a good selection to estimate the frequency of the turbulent fluctuations. However, the sensitivity of discrimination between turbulent and no turbulent fluctuations is limited because the spectra are similar for both cases. For the Bessel distribution with w_N = 2-ms rectangular windows and $\alpha = 2$, the bandwidths of the Kolmogorov spectra are smaller than the simulated one. However, the difference is emphasized between the case of turbulence and no turbulence. The right panels show the results for parameters optimized to measure the magnitude of the turbulent fluctuations. As seen, the Kolmogorov bandwidths are much smaller for these cases.

DISCUSSION

In an article by our group (Cloutier et al. 1996), blood flow turbulence downstream of a stenosis was measured by using pulsed-wave Doppler US. No measurement of the Kolmogorov spectrum was performed in that study. The velocity fluctuations were assessed at several locations after the stenosis and hot-film anemometry was used to validate the spatial distribution of the turbulence intensity. Although the relative changes in turbulence and the position of the peak downstream of the stenosis were correctly mapped, significant overestimation of the intensity (more than 5 times) was noted when comparing the results to hot-film anemometry. It was suggested that velocity-independent instrument noise, the relatively large size of the Doppler sample volume, and instability of the flow in the model could explain these results. In this study, the Doppler spectra were processed by using *AR* modeling over 2-ms rectangular windows (the *AR* model was the same as the one

used here). According to Fig. 6, this window length is not optimum to minimize the variance of the spectral estimator and to measure the magnitude of the turbulent fluctuations. Thus, the intrinsic variance of the *AR* spectral estimator could have contributed to the unexpected high turbulence intensities measured in our previous study (Cloutier et al. 1996). The use of a 10-ms rectangular window instead of the 2-ms window would have improved the accuracy of the results.

In other previous studies (Giddens and Khalifa 1982; Nygaard et al. 1994a), the approaches used to measure *in vivo* the velocity fluctuations with US differed significantly from the methods tested here. The comparison of our results is, thus, difficult in this context. On the other hand, some investigators reported simulations aimed at evaluating the stability of TFR estimators to track the Doppler mean frequency. Kaluzynski and Palko (1993) tested the variance of the Doppler mean frequency estimated with two autoregressive algorithms as a function of the model order and window length. Sava et al. (1999) performed similar computations for a broader range of short-time spectral parametric methods (two *AR* models, the Prony method, and the Steiglitz–McBride autoregressive moving average method). In both studies, the results were compared to the standard short-time Fourier method. As noted in these studies, the variance increased when reducing the window length from 10 to 1 ms. Similar findings were found in the present study for the case of no turbulence (Figs. 5 to 9). In Kaluzynski and Palko (1993) and Sava et al. (1999), the selection of the *AR* model order had little effect for values in the range of 10 to 40. By varying the model order between 8 to 16, no significant effect on Mean_Abs_Freq_Dif was also noted in the present study.

As shown in Table 3, four algorithms provided similar biases to estimate Mean_Abs_Freq_Dif when there was no turbulence (*SPEC, AR, CWD* and *BD*). Although no statistical test was performed in their study, Sava et al. (1999) found that the method with the minimum variance, for a signal-to-noise (S:N) ratio greater than 10 decibels and window lengths varying between 1 and 10 ms, was *AR* (Levinson–Durbin algorithm and maximum entropy method) followed by the spectrogram. These results are consistent with those reported in Table 3. Guo et al. (1994b) computed the variance (normalized r.m.s. error) of the Doppler mean frequency for the short-time Fourier method, *AR* modeling, the Bessel distribution, the Choi–Williams distribution, and the Choi–Williams reduced interference distribution. The smallest errors, for S:N ratios of 10 decibels and higher, were obtained with the Bessel distribution for the optimum spectral parameters considered in that study (w_N = 4-ms sine-cosine windows and $\alpha = 16$). By using a 10-ms rectangular window and $\alpha = 16$, the Bessel distribution also was considered a good method to minimize the variance of the Doppler mean frequency (Table 3). As reported in the Results section, it was found that the sine-cosine window was slightly better than the rectangular window when the parameter Mean_Abs_Freq_Dif is considered. By using a 10-ms sine-cosine window, slightly better results could have been obtained by Guo et al. (1994b).

Some investigators suggested strategies to detect disturbed flow with Doppler ultrasound (Gaupp et al. 1999; Talhami and Kitney 1988; Wang and Fish 1996). These strategies were usually proposed as an alternative to the short-time Fourier algorithm. The maximum-likelihood Kalman model (an autoregressive moving average method) was used to track ramp-type variations and low-frequency sinusoidal oscillations (period of 4 ms, typically) of the Doppler mean frequency (Talhami and Kitney 1988). Although not specified in the study, the sinusoidal oscillations simulated during flow deceleration of the time-varying signal may correspond to large-scale vortex shedding. The performance of the Kalman model was better than the Fourier method for the situations considered. The detection of very large-scale deterministic vortices (period of 15 ms), as found during the deceleration of the flow in the carotid artery, was investigated with the short-time Fourier transform and a new FFT-based stationarizing algorithm, the *AR* covariance model, the pseudo-Wigner–Ville method, and the Choi–Williams algorithm (Wang and Fish 1996). For the spectral parameters considered, the stationarizing FFT-based algorithm provided the best detection of the large vortices. Moreover, the mean frequency estimated with the Choi–Williams distribution was shown to be insensitive to the choice of σ for values between 0.05 and 10. As noted in Fig. 7, a similar behavior was found for σ varying between 0.05 and 0.2. For $\sigma = 0.01$, we noted an effect on Mean_Abs_Freq_Dif as the window length was reduced. Recently, the same group characterized vortex shedding in vascular anastomosis models with the short-time Fourier transform (Gaupp et al. 1999). Deterministic vortices were detected with a time resolution of 2.5 ms.

As discussed earlier, the detection of random turbulent fluctuations covering a wide range of eddy sizes has not been addressed so far in the US literature. The present study may provide basic guidelines for selecting the optimal method and set of parameters for this purpose. According to Hinze (1975), the upper size limit of the eddies that can be detected is mainly determined by the size of the apparatus, whereas the lower limit is determined by viscosity effects and decreases with increasing velocity of the average flow. Consequently, for *in vivo* clinical assessment of the scale of turbulent motions with US, a key parameter to optimize is the size

of the Doppler sample volume. To our knowledge, the determination of the effect of the US sample volume size on the detectability of microscale turbulent motions has not been addressed so far in the literature. With the exception of the velocity vector perpendicular to the US beam, the Doppler modality is sensitive to the 3-D motion of the flow. However, more work should be conducted to understand the contribution of 3-D vortices smaller than the sample volume size on the Doppler spectrum. The advancement in high-frequency US and new beam-forming strategies may improve the detectability of microscale vortices by reducing the size of the sample volume. For cardiac applications, transesophageal echography may allow the use of high-frequency transducers.

CONCLUSION

An exhaustive evaluation of the performance of time-frequency representation techniques has been presented for applications related to the measurement of blood flow turbulence with US. For each technique, the parameters expected to provide adequate mapping of the magnitude and scale of the turbulent fluctuations were tested. To minimize the variance of the estimator and to measure the magnitude of the turbulent frequency fluctuations, four methods provided similar results: *SPEC* (10-ms sine-cosine windows), *AR* (10-ms rectangular windows, model order = 8), *CWD* (w_N and w_M = 10-ms rectangular windows, $\sigma = 0.01$), and *BD* (w_N = 10-ms rectangular windows, $\alpha = 16$). To measure the scale of the turbulent motions (Kolmogorov spectrum), the Bessel distribution gave the best results (w_N = 2-ms rectangular windows, $\alpha = 2$).

Because of the lack of information in the literature, no clear guideline could be used to select the optimal set of parameters for the application in hand (characterization of large vortices to microscale turbulent motions). In the current study, the range of window lengths has been limited to 1 to 10 ms. The shortest windows were used to optimize time resolution, whereas the upper limit of 10 ms was selected to respect the stationarity criterion of the Doppler blood flow signal (Guo et al. 1993). From the results of Figs. 5 to 9, the longest windows may also be a good selection to minimize the variance of the estimator and to measure the intensity of turbulence. The performance for longest windows still needs to be determined. It is clear that the conclusions drawn from this study may depend on the simulation model used. Further validation with *in vitro* and *in vivo* data would be necessary. The recognition of Doppler US as a precise means of measuring blood flow turbulence noninvasively will require further validation with "gold standards" such as hot-film or laser Doppler anemometry.

Acknowledgement—This work was supported by a research scholarship from the Fonds de la Recherche en Santé du Québec, and by a grant from the Natural Sciences and Engineering Research Council of Canada (grant #OGPIN 335). The authors acknowledge Drs. S. G. Mallat and Z. Zhang for providing the matching pursuit software.

REFERENCES

Butchart EG. Prosthetic heart valves. In: Verstraete M, Fuster V, Topol EJ, eds. Cardiovascular thrombosis: Thrombocardiology and thromboneurology. Philadelphia, New York: Lippincott - Raven, 1998:395–414.

Chesebro JH, Fuster V. Valvular heart disease and prosthetic heart valves. In: Verstraete M, Fuster V, Topol EJ, eds. Cardiovascular thrombosis: Thrombocardiology and thromboneurology. Philadelphia, New York: Lippincott-Raven, 1998:365–394.

Choi HI, Williams WJ. Improved time-frequency representation of multicomponent signals using exponential kernels. IEEE Trans Acoust Speech Signal Processing 1989;37:862–871.

Cloutier G, Allard L, Durand LG. Characterization of blood flow turbulence with pulsed-wave and power Doppler ultrasound imaging. J Biomech Eng 1996;118:318–325.

Fontaine AA, Heinrich RS, Walker PG, Pedersen EM, Scheidegger MB, Boesiger P, Walton SP, Yoganathan AP. Comparison of magnetic resonance imaging and laser Doppler anemometry velocity measurements downstream of replacement heart valves: Implications for in vivo assessment of prosthetic valve function. J Heart Valve Dis 1996;5:66–73.

Gaupp S, Wang Y, How TV, Fish PJ. Characterization of vortex shedding in vascular anstomosis models using pulsed Doppler ultrasound. J Biomech 1999;32:639–645.

Giddens DP, Khalifa AMA. Turbulence measurements with pulsed Doppler ultrasound employing a frequency tracking method. Ultrasound Med Biol 1982;8:427–437.

Guo Z, Durand LG, Allard L, Cloutier G, Lee HC, Langlois YE. Cardiac Doppler blood flow signal analysis. Part I: Evaluation of the normality and stationarity of the temporal signal. Med Biol Eng Comput 1993;31:237–241.

Guo Z, Durand LG, Lee HC. The time-frequency distributions of nonstationary signals based on a Bessel Kernel. IEEE Trans Signal Processing 1994a;42:1700–1707.

Guo Z, Durand LG, Lee HC. Comparison of time-frequency distribution techniques for analysis of simulated Doppler ultrasound signals of the femoral artery. IEEE Trans Biomed Eng 1994b;41:332–342.

Hinze JO. Turbulence. New York: McGraw-Hill, 1975.

Hung TC, Hochmuth RM, Joist JH, Suteras P. Shear-induced aggregation and lysis of platelets. Trans Am Soc Artif Intern Organs 1976;22:285–291.

Jeong J, Williams WJ. Alias-free generalized discrete-time time-frequency distributions. IEEE Trans Signal Processing 1992a;40:2757–2765.

Jeong J, Williams WJ. Kernel design for reduced interference distributions. IEEE Trans Signal Processing 1992b;40:402–412.

Kaluzynski K, Palko T. Effect of method and parameters of spectral analysis on selected indices of simulated Doppler spectra. Med Biol Eng Comput 1993;31:249–256.

Kay SM, Marple SL Jr. Spectrum analysis—A modern perspective. Proc IEEE 1981;69:1380–1419.

Kroll MH, Hellums JD, McIntire LV, Schafer AI, Moake JL. Platelets and shear stress. Blood 1996;88:1525–1541.

Mallat SG, Zhang Z. Matching pursuits with time-frequency dictionaries. IEEE Trans Signal Processing 1993;41:3397–3415.

Milnor WR. Hemodynamics. Baltimore, Hong Kong, London, Sydney: Williams & Wilkins, 1989.

Mo LYL, Cobbold RSC. A nonstationary signal simulation model for continuous wave and pulsed Doppler ultrasound. IEEE Trans Ultrason Ferroelec Freq Cont 1989;36:522–530.

Nichols WW, O'Rourke MF. McDonald's blood flow in arteries. Theoretical, experimental and clinical principles. Philadelphia, London: Lea & Febiger, 1990.

Nygaard H. Quantitative evaluation of turbulence downstream of aortic

valves with special reference to patients with stenotic and prosthetic aortic valves. Aarhus University Hospital, Ph.D. Thesis, 1994.

Nygaard H, Hasenkam JM, Pedersen EM, Kim WY, Paulsen PK. A new perivascular multi-element pulsed Doppler ultrasound system for in vivo studies of velocity fields and turbulent stresses in large vessels. Med Biol Eng Comput 1994a;32:55–62.

Nygaard H, Paulsen PK, Hasenkam JM, Kromann-Hansen O, Pedersen EM, Rovsing PE. Quantitation of the turbulent stress distribution downstream of normal, diseased and artificial aortic valves in humans. Eur J Cardio-thorac Surg 1992;6:609–617.

Nygaard H, Paulsen PK, Hasenkam JM, Pedersen EM, Rovsing PE. Turbulent stresses downstream of three mechanical aortic valve prostheses in human beings. J Thorac Cardiovasc Surg 1994b;107: 438–446.

Sallam AM, Hwang NHC. Human red blood cell hemolysis in a turbulent shear flow: Contribution of Reynolds shear stresses. Biorheology 1984;21:783–797.

Sava H, Durand LG, Cloutier G. Performance of short-time spectral parametric methods for reducing the variance of the Doppler ultrasound mean instantaneous frequency estimation. Med Biol Eng Comput 1999;37:291–297.

Shen SF. Some considerations on the laminar stability of time-dependent basic flows. J Aerospace Sci 1961;28:397–404, 417.

Stein PD, Sabbah HN, Pitha JV. Continuing disease process of calcific aortic stenosis. Role of microthrombi and turbulent flow. Am J Cardiol 1977;39:159–163.

Talhami HE, Kitney RI. Maximum likelihood frequency tracking of the audio pulsed Doppler ultrasound signal using a Kalman filter. Ultrasound Med Biol 1988;14:599–609.

Talukder N, Fulenwider JT, Mabon RF, Giddens DP. Poststenotic flow disturbance in the dog aorta as measured with pulsed Doppler ultrasound. J Biomech Eng 1986;108:259–265.

Walker PG, Pedersen EM, Oyre S, Flepp L, Ringaard S, Heinrich RS, Walton SP, Hasenkam JM, Jorgensen HS, Yoganathan AP. Magnetic resonance velocity imaging: A new method for prosthetic heart valve study. J Heart Valve Dis 1995;4:296–307.

Wang Y, Fish PJ. Comparison of Doppler signal analysis techniques for velocity waveform, turbulence and vortex measurement: A simulation study. Ultrasound Med Biol 1996;22:635–649.

Welch PD. The use of fast Fourier transform for the estimation of power spectra: A method based on time averaging over short, modified periodograms. IEEE Trans Audio Electroacoust 1967;15: 70–73.